Focal Plane Array Based on HgTe Nanocrystals with Photovoltaic Operation in the Short-Wave Infrared

Rodolphe Alchaar, Adrien Khalili, Nicolas Ledos, Tung Huu Dang, Maxime Lebreton, Mariarosa Cavallo, Erwan Bossavit, Huichen Zhang, Yoann Prado, Xavier Lafosse, et al.

Focal Plane Array Based on HgTe Nanocrystals with Photovoltaic Operation in the Short-Wave Infrared

Rodolphe Alchaar[1], Adrien Khalili[1], Nicolas Ledos[1], Tung Huu Dang[1,2], Maxime Lebreton [2], Mariarosa Cavallo[1], Erwan Bossavit[1], Huichen Zhang[1], Yoann Prado[1], Xavier Lafosse[3,] Victor Parahyba[4], Pierre Potet[4], David Darson[2], Emmanuel Lhuillier[1*]

[1] Sorbonne Université, CNRS, Institut des NanoSciences de Paris, INSP, F-75005 Paris, France.
[2] Laboratoire de Physique de l'Ecole normale supérieure, ENS, Université PSL, CNRS, Sorbonne Université, Université Paris Cité, 75005 Paris, France.
[3]Centre de Nanosciences et de Nanotechnologies, CNRS, Univ. Paris-Sud, Université Paris-Saclay, 10 Boulevard Thomas Gobert, 91120 Palaiseau, France
[4] New Imaging Technologies SA, 1 impasse de la Noisette 91370 Verrières le Buisson, France.

Abstract: Thanks to their remarkable spectral tunability across the entire infrared range, HgTe nanocrystals present a unique platform for designing infrared optoelectronic devices. While in recent years, most of the significant advances in this domain have been made on devices at the single-pixel level, there is a growing trend toward exploring the potential of this material for imaging applications. However, until recently, focal plane arrays based on HgTe NCs have been limited to the photoconductive mode, which is inherently associated with a large dark current. In this work, we demonstrate a diode stack compatible with a read-out integrated circuit whose back-end processing has been optimized to ensure compatibility with a complete diode stack deposition. The diode design is also optimized to generate a Fabry-Perot cavity in which 50 % of the light is effectively absorbed at the band edge. Finally, taking benefit from the full VGA format, high-resolution images are taken.

Keywords: nanocrystals, HgTe, infrared, photodiode, focal plane array, imaging.

*To whom correspondence should be sent: el@insp.upmc.fr

Colloidal nanocrystals (NCs) can operate at wavelengths beyond the bandgap of silicon[1,2] by exploiting their inorganic nature and broadly tunable optical properties. In this spectral range, current technologies are prohibitively expensive for mass-market applications, and organic materials are ineffective due to the strong coupling between excitons and molecular vibrations. Among candidate materials, PbS and HgTe have been extensively studied to generate infrared photoconduction and have already been integrated into more advanced devices such as photodiodes[3–5], phototransistors[6–8], light modulators[9], spectrometers[10,11], devices coupled to light resonators [12–15], and imagers[16–20].

The development of PbS-based solar cells has led to the effective transfer of this material into photodiode arrays, including at an industrial scale[16–18]. However, this yet to be the case for HgTe,[21,22] which in fact presents several advantages compared to PbS, such as a more tunable absorption edge to explore the short, mid[23] and long[24,25] wave infrared, and a reduced susceptibility to oxidation[26]. Moreover, efficient photodiode reports remain fairly recent[3,5,27–31] and thus most of the reported focal plane arrays (FPA) based on HgTe NCs rely on the photoconductive operation[19,20]. While this approach simplifies fabrication by reducing the number of steps, the lack of any built-in electric field enforces the need to apply bias, resulting in the generation of a dark current and its consequent reduction of the signal-to-noise ratio. Recent efforts have focused on the design of single-pixel HgTe NCs-based photodiodes that now reach high detectivity values of around 10^{11} Jones for short-wave infrared operation at room temperature[3,5,27–30]. However, transferring those diodes to FPA structures requires updates to the read-out integrated circuit's (ROIC) morphology and possibly to the diode design. Mainly, there is a need to take into account the fact that illumination can no longer occur through the substrate. In this paper, we explore the design of an HgTe NCs photodiode array with a 1.9 µm cut-off wavelength.

To build a photodiode using HgTe NCs, we use a diode stack similar to the one proposed by Greboval *et al.*[27] relying on an FTO (fluorine-doped tin oxide)/SnO_2/HgTe/Ag_2Te/Au structure, see **Figure 1**c. This particular stack can be operated in either an inverted or a non-inverted configuration, a critical feature for its subsequent transfer to a ROIC. In this stack, the Ag_2Te layer is used as the hole transport layer, while the SnO_2 layer acts as the electron extractor. The absorbing HgTe NCs are grown using Keuleyan's procedure in which $HgCl_2$ is reacted with trioctylphosphine telluride in oleylamine. The temperature (58°C) and duration (3 min) are chosen so that the final material presents an exciton at 1.65 µm, see **Figure 1**a. The resulting particles have a branched aspect and a typical size in the 6-8 nm range according to transmission electron microscopy, see **Figure 1**b. After deposition, the ligands in the material are exchanged to render the film electrically conductive, which also shifts the photoconductive properties to longer wavelengths, resulting in a cut-off wavelength of 1.9 µm, see **Figure 1**d. This wavelength is chosen to highlight the benefit of nanocrystals compared to the InGaAs alloy, which also exhibits some spectral tunability in this range, but at the cost of lattice mismatch with the InP substrate. With NCs, however, the constraint of epitaxy is lifted, allowing for the continuous tuning of the particle size and thus of the associated bandgap in the short-wave infrared (2 µm cut-off) and extended short-wave infrared (2.5 µm cut-off). The device presents a strongly rectifying IV curve even for room temperature operation, see **Figure 1**e, with three orders of magnitude of difference in the current asymmetry under 0.4 V bias operation. Under reverse bias, the current presents a limited hysteresis as bias with bias sweep direction. This behavior is absent under illumination since the photocurrent prevails over any parasitic effect such as ions migration. Under illumination with 4 mW of incident power, we observe an open circuit voltage of 250 mV (*1/3* of the bandgap). This diode stack also exhibits fast operation, with a 90-10 % decay time of the photocurrent of approximately 3 µs after illumination by a 1 ns-long pulse at 1.57 µm, for a 1 mm^2 diode size.

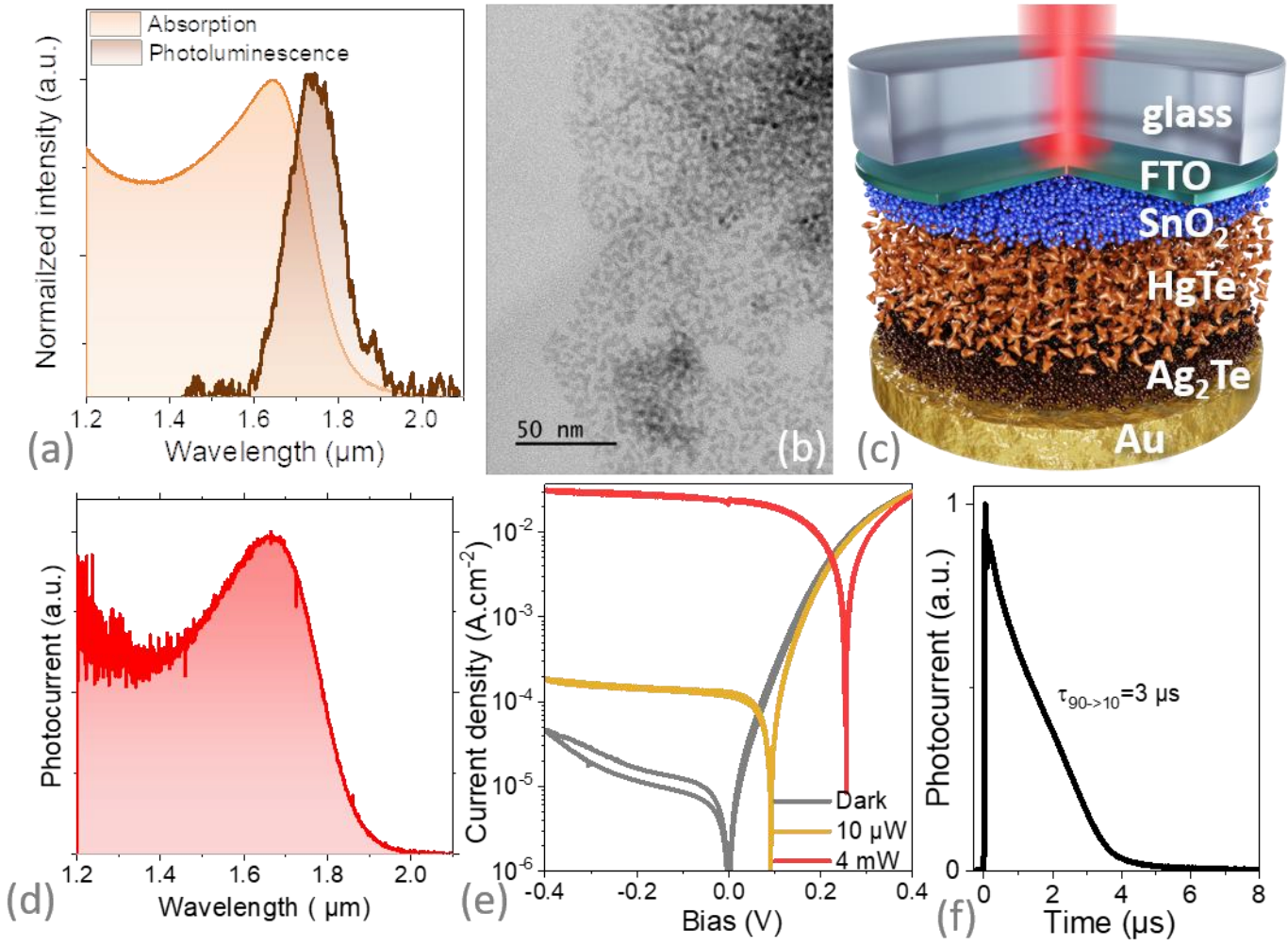

***Figure 1 Single pixel diode**. a. Absorption and photoluminescence spectra of the HgTe NCs with a cut-off wavelength at 1.9 µm. b. TEM image of the HgTe NCs. c. Schematic of the diode stack used for SWIR sensing. d. Photocurrent spectrum measured at 0 V and room temperature. e. IV curves of the photodiode stack depicted in part c under dark conditions and under illumination by a laser diode (λ=1.55 µm). e. Photocurrent as a function of time after illumination by a 1 ns-long pulse at 1.57 µm.*

For device area of 1 mm^2, the measured responsivity was 290 $mA.W^{-1}$, corresponding to an external quantum efficiency of 23 % (Figure S1). Under 0 V bias, the noise in this diode stack follows a white noise profile, see Figure S2. The specific detectivity, defined as the ratio of the responsivity over the current spectral noise density and normalized by the square root of the optical area, is $1.2x10^{11}$ Jones at room temperature. The detectivity can be further increased by operating the device at reduced temperatures, as this reduces the number of thermally activated carriers. Specifically, the detectivity can be increased to $3.9x10^{11}$ Jones and $2x10^{12}$ Jones at 250 K and 200 K, respectively. Now that a diode stack with high performance is established, we aim to transfer it onto a ROIC.

This process presents several challenges. Firstly, the presence of the ROIC prevents illumination from the bottom side. Secondly, the overall diode stack thickness falls within the 200 to 500 nm range, which requires the ROIC to present an excellent surface smoothness to avoid the formation of cracks and their associated electrical short. Furthermore, the usual deposition of the FTO electrode, done at a high temperature (500°C) by chemical growth, is incompatible with the HgTe NCs, that poorly sustain exposure to high temperatures[26]. Lastly, it has been pointed out by Alchaar *et al.*[32] that some metals, such as Ag, are prompt to form an amalgam with HgTe NCs. This is why

we choose to replace the typical transparent top electrode by a thin gold layer in the present work, which raises both opportunities and concerns, as discussed later.

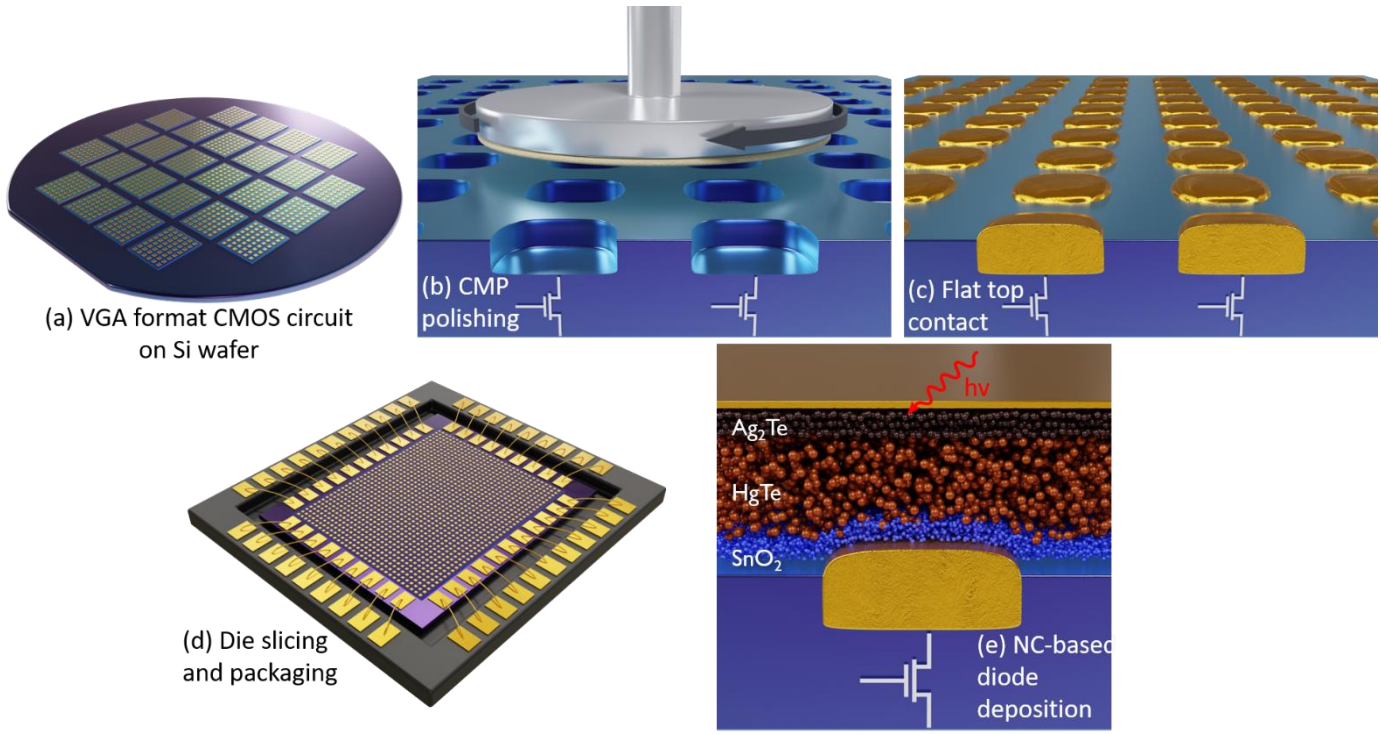

***Figure 2 Fabrication of the photodiode array**. (a). Step one is dedicated to the VGA format array that is fabricated on an 8 inches wafer. (b). This wafer is then polished to obtain a flat surface. (c). Electrode contacts are grown with a top gold plating to minimize amalgam formation with the HgTe NCs deposited later. (d). The wafer is then sliced and packaged. (e). The diode stack is deposited by spin coating; the top Au electrode is 20 nm thick and thus is semi-transparent.*

The photodiode array is fabricated as described in **Figure 2**. First, VGA format ROICs (640x512 pixels - model NITquantum c) with 15 µm pixel pitch are provided from a silicon foundry (**Figure 2**a). In order to obtain a flat surface, the wafers are polished using mechanical polishing (**Figure 2**b). Then, for each pixel, a gold electrode is grown with a thickness chosen so that the final electrode slightly protrudes from the surface of the dielectric, see Figure S3-4. The circuits are then sliced and packaged onto a ceramic chip carrier, see **Figure 2**d. Finally, the same diode stack as the one depicted in **Figure 1** is deposited via spin coating. To ensure some transparency of the top metallic electrode, the thickness is set at approximately 20 nm, see Figure S4. Following fabrication, the sample is kept in the air without further protection against oxidation.

In this chosen configuration, the active layer of the diode is sandwiched between two gold layers, which favors the formation of a Fabry Perot cavity. Thus, the diode thickness can be optimized generate a resonance that matches the HgTe bandgap. This strategy to shape the spectral response comes in addition to the material band gap tunability and thus offers flexibility in the final shaping of the spectral response. In a text book Fabry Perot cavity, the resonance condition is given by $nL=m\lambda/2$, with n the refractive index of the cavity, L the cavity length, m an integer, and λ the wavelength. The refractive index of HgTe after ligand exchange[33] being close to 2.3 (see Figure S5-6), a resonance around 1.7 µm should be obtained for a thickness of 180 nm. In order to get a more accurate estimation of the device absorption while considering the properties of the other layers, we have conducted an electromagnetic simulation using finite element simulation. The simulation of the effective device absorption (i.e., the absorption in the NC layer and excluding metallic contacts) shows a resonance that matches the band edge for a HgTe NCs layer thickness of 200 nm. Further increasing the absorbing layer's thickness does not enhance the absorption at the band edge but only at higher energies, see **Figure 3**a. Consequently, a 200 nm thick HgTe layer has been targeted. In this case, the absorption can reach 50 %, whereas, without the resonance, such a layer should

only absorb 10 % of the incident light. The drawback of this approach is the strong optical loss occurring in the top metallic contact, see **Figure 3**b and c, which can reach 60 % near the cut-off wavelength. For comparison, we also have simulated the diode stack where the top metal contact is replaced by a thin ITO layer (50 nm thickness, see Figure S7). In this case, the absorption drops by a factor 2 (around 25 % of the incident light), but the losses are also drastically reduced (4 % at the resonance). These results point toward the need to determine the most effective strategies.

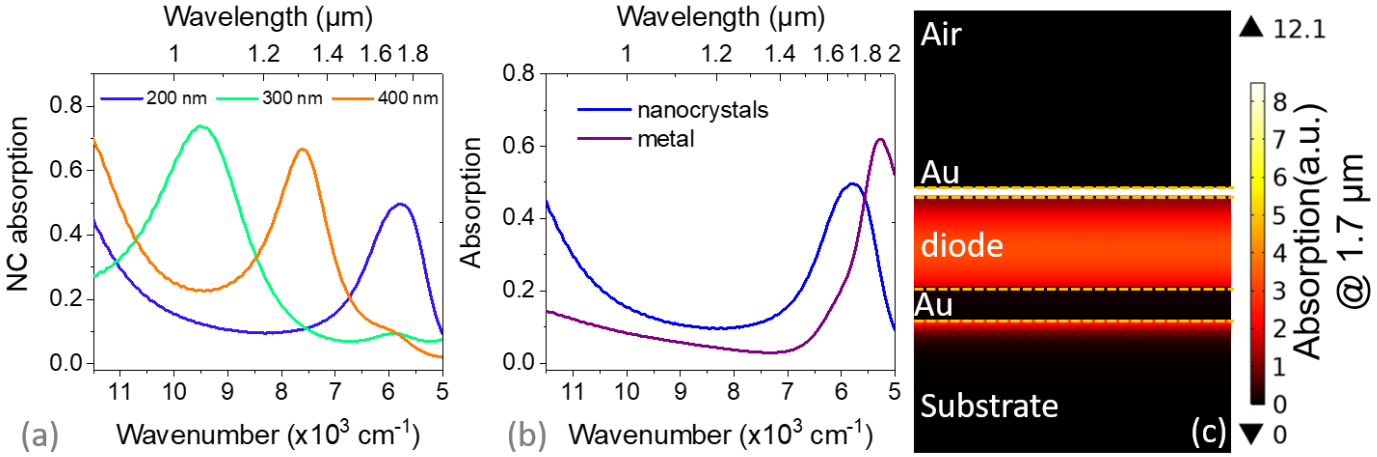

Figure 3 Simulated optical properties of the diode stack. *a. Simulated absorption spectra within the NCs for three thicknesses of the HgTe layers. b. Simulated absorption spectra in gold and in the NCs for a 200 nm thick diode stack. c. Absorption map of the diode same stack at 1.7 μm (i.e., around the resonant wavelength).*

The potential of the diode for SWIR imaging is then evaluated, see **Figure 4**a and b. A comparison is made between the visible and infrared images of a scene, emphasizing the contrast of some elements. Water, typically transparent in the visible, appears dark in SWIR imaging due to its absorption band around 1400 nm, as does the ITO substrate. However, the Si wafer becomes transparent due to its bandgap located around 1200 nm. The promising potential of this technology for thermal imaging is highlighted by the strong signal resulting from the warm soldering iron in the back. Note that contrary to our previous demonstrations based on a planar photoconductive operation[19], where polarization required the use of one pixel out of two, the vertical transport in this device allows us to take advantage of the entire VGA format. Thus, the image resolution is improved compared to the photoconductor, which is better highlighted by imaging a test chart in **Figure 4**d or a face in **Figure 4**c.

The benefit of the photovoltaic operation compared to the photoconductive mode is further illustrated by tracking the dark current histogram, see **Figure 4**e. In the ROIC, the reading capacitance is around C=170 ke$^-$. If we assume that the saturation of the signal, in analog digital units corresponds to a full filling of the capacitance (C/t_i=adu range, with t_i the integration time and adu range the saturating signal≈45 000, see **Figure 4**e), we can estimate the dark current to be around 10 pA for a 10 ms integration time. Since the pixel size is 15x15 μm^2, the dark current density at -40°C is 4 μA.cm^{-2}, a value in the same range as the one observed for the single-pixel device, see **Figure 1**e. Furthermore, by taking advantage of the built-in electric field of the diode structure, a reduced driving voltage can be applied. Thus, the lower dark current and operating voltage enable longer integration times (tens of ms) compared to the photoconductive mode, where the dark current saturates the read-out capacitance for exposure times longer than a few hundred μs for the same active layer[19]. By cooling the device to -40 °C (using a double Pelletier stage), an even higher integration time of 50 ms can be achieved without saturation.

Finally, since the output signal is digitized over 16 bits, we can determine the external quantum efficiency (EQE) by tracking the photocurrent signal as a function of incident illumination power. The EQE relates to the slope of the signal vs. power graph and is determined by comparing the slope (Figure S8) with the one obtained for InGaAs, for which an EQE of 90 % has been previously determined. We obtain a modest value of 0.33 % at 1.55 µm. The reading noise of this ROIC is around 60 electrons per frame, while using a gain of 1.7 electron/adu, meaning that the dynamic range is 58 dB. The large optical losses in the top metallic contact are, in part, responsible for this value. Another clear reason can be attributed to the use of gold as the top contact, which tends to limit the diode asymmetry. A previous study has shown that using gold on both sides of the diode reduces the open circuit voltage by a factor of 2 compared to the case where FTO and gold are used[32]. Comparatively, the diode with a top ITO contact, which has a reduced absorption, achieves an EQE almost double (0.6 %, see Figure S9). Though such better value remains far lower than what is to date achieved for PbS NC-based imager, for which 2 µm cut off device achieves 15 % EQE[34]. The performances achieved at the single pixel level, make us nevertheless believe that the issue is purely technological and that far higher performances matching PbS can be obtained with HgTe NCs.

At this stage, performances are still limited by the electrical properties of the diode stack rather than by absorption. Therefore, future development efforts must focus on designing a top contact to address these performance bottlenecks. Certainly, the use of gold (which has a large work function) as the electrode on the electron extraction side is also sub-optimal. However, currently, gold is used for its chemical stability since, as mentioned previously, it has been observed that some metals tend to form amalgams with Hg[32].

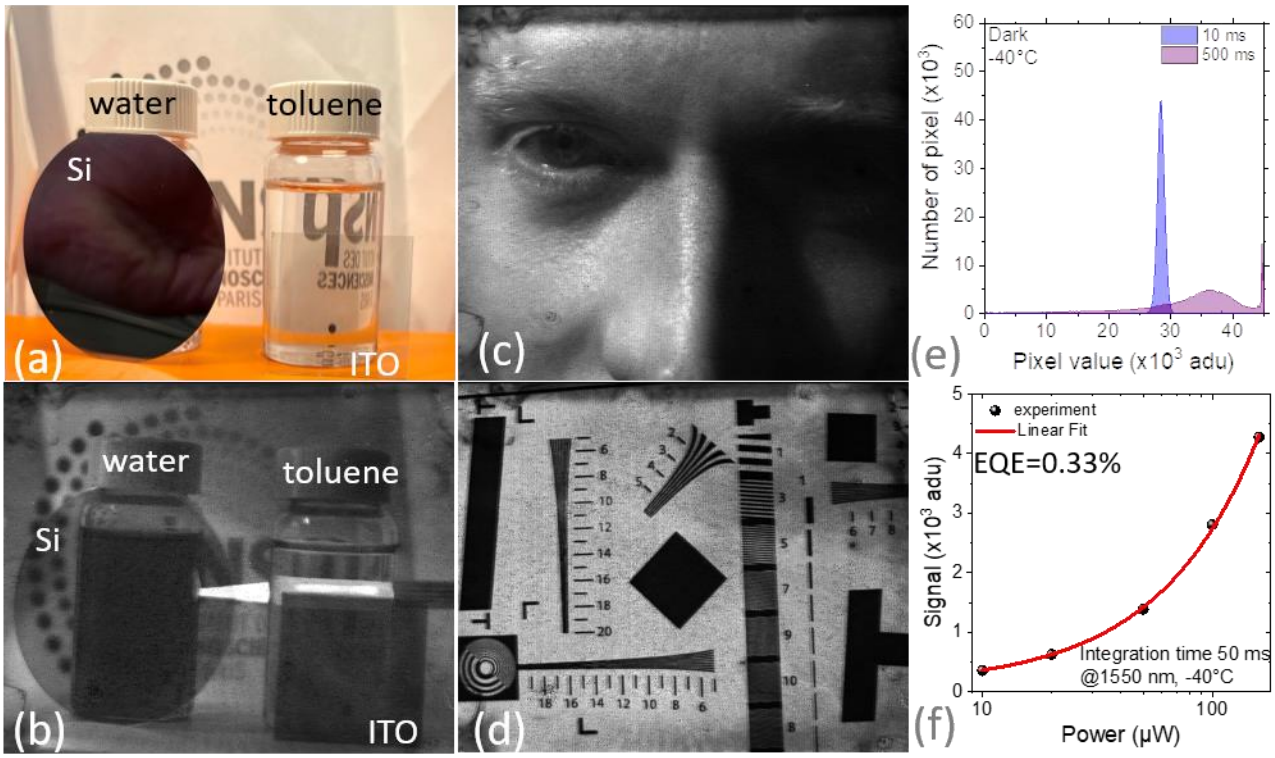

Figure 4 Imaging using HgTe NC based photodiode array*. a. Visible image of a scene captured by the 12 megapixels detector of a smartphone (Iphone 12 pro with f/2 aperture and 52 mm equivalent focal length). Images acquired with the HgTe NC diode array of b. the same scene as part a, and behind which a hot soldering iron tip (300 °C) has been added, c. the last author's face, and d. an ISO12233:2000 for measuring the resolution of electronic still-picture cameras. e. Histogram of the dark current level for various integration time. f. Photocurrent signal measured in adu (analog-to-digital units) as a function of incident light power of a 1.55 µm laser diode. From the*

slope of this graph, we extract an EQE of 0.33 % at 1550 nm. All infrared images and data are obtained at -40°C.

In conclusion, we demonstrate a photodiode array with HgTe nanocrystals as the active layer. Compared to conventional InGaAs alloy, the diode offers an extended photoresponse of up to 1.9 µm and is fully compatible with air exposure. Compared to the single-pixel device, the transfer to the focal plane array level has been achieved by a surface modification of the ROIC, not only by bringing the roughness below the diode thickness but also by a proper choice of metal that prevents amalgam formation. The diode thickness is optimized to generate a Fabry-Perot cavity that enables effective absorption of up to 50 % at the NC band edge. Present performances remain limited with an EQE below 1 %, and future efforts will have to focus on the optimization of the top contact design as well as the electron extraction.

SUPPORTING INFORMATION

Supporting Information include details about (*i*) noise measurement (*ii*) characterization of the photodiode array morphology, (*iii*) Electromagnetic simulation of the absorption and (*iv*) EQE estimation at the FPA level.

ACKNOWLEDGEMENTS

The project is supported by ERC grant blackQD (grant n° 756225) and AQDtive (grant n°101086358). We acknowledge the use of clean-room facilities from the “Centrale de Proximité Paris-Centre” and the french RENATECH network. This work was supported by Agence Nationale de la recherche through the grants Copin (ANR-19-CE24-0022), Frontal (ANR-19-CE09-0017), Graskop (ANR-19-CE09-0026), NITQuantum (ANR-20-ASTR-0008), Bright (ANR-21-CE24-0012), MixDFerro (ANR-21-CE09-0029) and Quicktera (ANR-22-CE09-0018).

CONFLICT OF INTEREST

The authors declare no competing financial interest.

Data availability

The data that support the findings of this study are available from the corresponding author upon reasonable request.

REFERENCES

[1] X. Zhao, G. Mu, X. Tang, and M. Chen, *Coatings* **12**, 467 (2022).
[2] T. Nakotte, S.G. Munyan, J.W. Murphy, S.A. Hawks, S. Kang, J. Han, and A.M. Hiszpanski, *J. Mater. Chem. C* **10**, 790–804 (2022).
[3] M. Chen, X. Xue, T. Qin, C. Wen, Q. Hao, and X. Tang, *Adv. Mater. Technol.*, 2300315 (2023).
[4] C.-H.M. Chuang, P.R. Brown, V. Bulović, and M.G. Bawendi, *Nat. Mater*. **13**, 796–801 (2014).
[5] M.M. Ackerman, X. Tang, and P. Guyot-Sionnest, *ACS Nano* **12**, 7264–7271 (2018).
[6] M.J. Grotevent, C.U. Hail, S. Yakunin, D. Bachmann, M. Calame, D. Poulikakos, M.V. Kovalenko, and I. Shorubalko, *Adv. Sci.* **8**, 2003360 (2021).
[7] C. Gréboval, A. Chu, D.V. Magalhaes, J. Ramade, J. Qu, P. Rastogi, A. Khalili, S.-S. Chee, H. Aubin, G. Vincent, S. Bals, C. Delerue, and E. Lhuillier, *ACS Photonics* **8**, 259–268 (2021).
[8] Y. Dong, M. Chen, W.K. Yiu, Q. Zhu, G. Zhou, S.V. Kershaw, N. Ke, C.P. Wong, A.L. Rogach, and N. Zhao, *Adv. Sci.* **7**, 2000068 (2020).

[9] H. Zhang, V. Guilloux, E. Bossavit, N. Fu, C. Dabard, M. Cavallo, T.H. Dang, A. Khalili, C. Abadie, R. Alchaar, C. Gréboval, X.Z. Xu, J.K. Utterback, D. Pierucci, S. Ithurria, J.I. Climente, T. Barisien, and E. Lhuillier, *ACS Photonics* **10**, 430–436 (2023).
[10] M.J. Grotevent, S. Yakunin, D. Bachmann, C. Romero, J.R. Vázquez de Aldana, M. Madi, M. Calame, M.V. Kovalenko, and I. Shorubalko, *Nat. Photonics* **17**, 59–64 (2023).
[11] C. Wen, X. Zhao, G. Mu, M. Chen, and X. Tang, *Coatings* **12**, 888 (2022).
[12] X. Tang, M.M. Ackerman, and P. Guyot-Sionnest, *Laser Photonics Rev.* **13**, 1900165 (2019).
[13] M. Chen, L. Lu, H. Yu, C. Li, and N. Zhao, *Adv. Sci.* **8**, 2101560 (2021).
[14] C. Abadie, L. Paggi, A. Fabas, A. Khalili, T.H. Dang, C. Dabard, M. Cavallo, R. Alchaar, H. Zhang, Y. Prado, N. Bardou, C. Dupuis, X.Z. Xu, S. Ithurria, D. Pierucci, J.K. Utterback, B. Fix, G. Vincent, P. Bouchon, and E. Lhuillier, *Nano Lett.* **22**, 8779–8785 (2022).
[15] T.H. Dang, C. Abadie, A. Khalili, C. Gréboval, H. Zhang, Y. Prado, X.Z. Xu, D. Gacemi, A. Descamps-Mandine, S. Ithurria, Y. Todorov, C. Sirtori, A. Vasanelli, and E. Lhuillier, *Adv. Opt. Mater.* **10**, 2200297 (2022).
[16] V. Pejovic, E. Georgitzikis, J. Lee, I. Lieberman, D. Cheyns, P. Heremans, and P.E. Malinowski, *IEEE Trans. Electron Devices* **69**, 2840–2850 (2022).
[17] V. Pejović, E. Georgitzikis, I. Lieberman, P.E. Malinowski, P. Heremans, and D. Cheyns, Adv. Funct. Mater. **32**, 2201424 (2022).
[18] J.S. Steckel, E. Josse, A.G. Pattantyus-Abraham, M. Bidaud, B. Mortini, H. Bilgen, O. Arnaud, S. Allegret-Maret, F. Saguin, L. Mazet, S. Lhostis, T. Berger, K. Haxaire, L.L. Chapelon, L. Parmigiani, P. Gouraud, M. Brihoum, P. Bar, M. Guillermet, S. Favreau, R. Duru, J. Fantuz, S. Ricq, D. Ney, I. Hammad, D. Roy, A. Arnaud, B. Vianne, G. Nayak, N. Virollet, V. Farys, P. Malinge, A. Tournier, F. Lalanne, A. Crocherie, J. Galvier, S. Rabary, O. Noblanc, H. Wehbe-Alause, S. Acharya, A. Singh, J. Meitzner, D. Aher, H. Yang, J. Romero, B. Chen, C. Hsu, K.C. Cheng, Y. Chang, M. Sarmiento, C. Grange, E. Mazaleyrat, and K. Rochereau, in *2021 IEEE Int. Electron Devices Meet. IEDM* (IEEE, San Francisco, CA, USA, 2021), p. 23.4.1-23.4.4.
[19] C. Gréboval, D. Darson, V. Parahyba, R. Alchaar, C. Abadie, V. Noguier, S. Ferré, E. Izquierdo, A. Khalili, Y. Prado, P. Potet, and E. Lhuillier, *Nanoscale* **14**, 9359–9368 (2022).
[20] S. Zhang, C. Bi, T. Qin, Y. Liu, J. Cao, J. Song, Y. Huo, M. Chen, Q. Hao, and X. Tang, *ACS Photonics* **10**, 673–682 (2023).
[21] C. Gréboval, A. Chu, N. Goubet, C. Livache, S. Ithurria, and E. Lhuillier, *Chem. Rev*. **121**, 3627–3700 (2021).
[22] Y. Tian, H. Luo, M. Chen, C. Li, S.V. Kershaw, R. Zhang, and A.L. Rogach, *Nanoscale* **15**, 6476–6504 (2023).
[23] S. Keuleyan, E. Lhuillier, V. Brajuskovic, and P. Guyot-Sionnest, *Nat. Photonics* **5**, 489–493 (2011).
[24] H. Zhang, J.C. Peterson, and P. Guyot-Sionnest, *ACS Nano* 17, 7530–7538 (2023).
[25] S. Pierini, F. Capitani, M. Scimeca, S. Kozlov, D. Pierucci, R. Alchaar, C. Abadie, A. Khalili, M. Cavallo, T.H. Dang, H. Zhang, E. Bossavit, C. Gréboval, J. Avila, B. Baptiste, S. Klotz, A. Sahu, C. Feuillet-Palma, X.Z. Xu, A. Ouerghi, S. Ithurria, J.K. Utterback, S. Sauvage, and E. Lhuillier, *J. Phys. Chem. Lett.* **13**, 6919–6926 (2022).
[26] H. Zhang, R. Alchaar, Y. Prado, A. Khalili, C. Gréboval, M. Cavallo, E. Bossavit, C. Dabard, T.H. Dang, C. Abadie, C. Methivier, D. Darson, V. Parahyba, P. Potet, J. Ramade, M.G. Silly, J.K. Utterback, D. Pierucci, S. Ithurria, and E. Lhuillier, *Chem. Mater.* **34**, 10964–10972 (2022).
[27] C. Gréboval, E. Izquierdo, C. Abadie, A. Khalili, M. Cavallo, A. Chu, T.H. Dang, H. Zhang, X. Lafosse, M. Rosticher, X.Z. Xu, A. Descamps-Mandine, A. Ouerghi, M.G. Silly, S. Ithurria, and E. Lhuillier, *ACS Appl. Nano Mater.* **5**, 8602–8611 (2022).
[28] P. Rastogi, E. Izquierdo, C. Gréboval, M. Cavallo, A. Chu, T.H. Dang, A. Khalili, C. Abadie, R. Alchaar, S. Pierini, H. Cruguel, N. Witkowski, J.K. Utterback, T. Brule, X.Z. Xu, P. Hollander, A. Ouerghi, B. Gallas, M.G. Silly, and E. Lhuillier, *J. Phys. Chem. C* **126**, 13720–13728 (2022).
[29] X. Xue, M. Chen, Y. Luo, T. Qin, X. Tang, and Q. Hao, Light Sci. Appl. **12**, 2 (2023).
[30] J. Yang, Y. Lv, Z. He, B. Wang, S. Chen, F. Xiao, H. Hu, M. Yu, H. Liu, X. Lan, H.-Y. Hsu, H. Song, and J. Tang, *ACS Photonics*, in press (2023).
[31] S. Günes, H. Neugebauer, N.S. Sariciftci, J. Roither, M. Kovalenko, G. Pillwein, and W. Heiss, *Adv. Funct. Mater.* **16**, 1095–1099 (2006).

[32] R. Alchaar, C. Dabard, D. Mastrippolito, E. Bossavit, T.H. Dang, M. Cavallo, A. Khalili, H. Zhang, L. Domenach, N. Ledos, Y. Prado, D. Troadec, M. Tallarida, F. Bisti, F. Cadiz, G. Patriarche, J. Avila, E. Lhuillier, and D. Pierucci, *J. Phys. Chem. C* asap (2023).
[33] P. Rastogi, A. Chu, T.H. Dang, Y. Prado, C. Gréboval, J. Qu, C. Dabard, A. Khalili, E. Dandeu, B. Fix, X.Z. Xu, S. Ithurria, G. Vincent, B. Gallas, and E. Lhuillier, *Adv. Opt. Mater*. **9**, 2002066 (2021).
[34] "Quantum Dot SWIR Cameras, http://image-sensors-world.blogspot.com/2018/11/quantum-dot-swir-cameras.html," visited on 6/22/2023.